***PREPRINT**: Journal of Hydrology 315(1-4): 252-273. (doi:10.1016/j.jhydrol.2005.03.029)* © Elsevier 2005

Numerical simulation of the wind-driven rainfall distribution over small-scale topography in space and time

Bert Blocken* [a], Jan Carmeliet [a,b], Jean Poesen [c]

(a) Department of Civil Engineering, Laboratory of Building Physics, K.U.Leuven, Kasteelpark Arenberg 40, 3001 Leuven, Belgium
(b) Faculty of Building and Architecture, Building Physics Group, T.U.Eindhoven, P.O. box 513, 5600 MB Eindhoven, The Netherlands
(c) Laboratory for Experimental Geomorphology, K.U.Leuven, Redingenstraat 16, 3000 Leuven, Belgium

*Author to whom correspondence should be addressed
Tel.: +32 (0) 16 32 13 45
Fax: +32 (0) 16 32 19 80
E-mail: bert.blocken@bwk.kuleuven.ac.be

Abstract

A general numerical simulation model is developed to determine the wind-driven rainfall (WDR) distribution over small-scale topography in space and time. It applies to the redistribution of rainfall by specific perturbed wind-flow patterns that occur over small-scale topography. The model is based on CFD (Computational Fluid Dynamics) and provides a necessary extension of the existing CFD models. It allows a high-resolution determination of the WDR distribution in both space and time. The model is demonstrated by application for a two-dimensional hill and a two-dimensional valley. The calculated distinct rainfall distribution patterns will be investigated and explained and the influence of different parameters will be analyzed in detail. It will be shown that the resulting variations in hydrologically effective rainfall can be very large (e.g. up to 92% in the examples analyzed). Therefore these variations should be taken into account in e.g. catchment hydrology, runoff and erosion studies and the design of rainfall monitoring networks.

Keywords: Rainfall redistribution; Hydrologically effective rainfall; Wind-flow pattern; Raindrop trajectories; Computational Fluid Dynamics; Driving rain.

1. Introduction

The influence of topography on rainfall distribution can be attributed to one of two different mechanisms: the orographic effect or the small-scale topographic effect. Both effects are driven by wind. The orographic effect acts on the meso-scale. It refers to the forced uplifting of moist air when approaching the windward slope of large hills or mountains. As the air cools below the dewpoint, water vapor condenses and precipitation is generated. When the partially dried air descends at the other side of the hill, it warms up and promotes evaporation. Because of this effect, the windward slope of large topographical configurations typically receives more rain than the leeward slope. On the other hand, the

wind-driven rain (WDR) topographic effect is a small or micro-scale effect (length from 0.1 m to several 1000s of meters and height from 0.1 m to several 100s of meters). This effect refers to the local and low-level redistribution of already generated rain due to the existence of specific local perturbed wind-flow patterns over small-scale topographical features. As such, it is not part of the rain producing process. Information from literature points out that these two effects are separable. James (1964), citing Geiger, mentions that the orographic effect does not come into play on low hills that are not a factor in the rising. He reports that, as ascending air cools with approximately 1° per 100 m of vertical rise, a hill less than 100 m higher than the surrounding area would not be subjected to this effect. On the other hand, the study by Poreh and Mechrez (1984) proves that the effect of large-scale topography on the redistribution of already generated rainfall is small.

The orographic effect has been quite adequately dealt with in literature (e.g. Haiden et al. 1992, Basist et al. 1994, Barrow and Lettenmeier 1994, to mention just a few). The small-scale topographical effect however has received less attention. Publications providing indications of the latter effect were provided by James (1964), Geiger (1965, p. 419) and Hovind (1965). They reported rainfall measurements that indicated the existence of relatively fixed rainfall distribution patterns. Later, further experimental research efforts adequately identifying the small-scale topographical effect were conducted by Sharon (1970), Sandsborg (1970), Reid (1973), Craig (1980), Sharon (1980, 1983), Sharon et al. (1988), Lentz et al. (1995) and Sharon and Arazi (1997).

Knowledge of the small-scale distribution of WDR is important for a wide range of activities in earth sciences and meteorology, including studies of catchment hydrology (e.g. Sharon 1970, Reid 1973), runoff and erosion studies (e.g. Sharon 1983, Poesen 1985, 1986, 1988, Sharon et al. 1988, Goossens et al. 2000, Erpul et al. 2002, 2003), the design of rainfall monitoring networks (e.g. Hutchinson 1970) and the selection of representative positions for rainfall measurements (e.g. Fourcade 1942, Hamilton 1954, de Lima 1990). The rainfall distribution patterns are often too complex to be predicted without measurements or numerical modeling. Measurements, if conducted with care, can provide accurate information. Such a study was carried out by Sharon and Arazi (1997) to study the rainfall distribution in a small watershed. However, for general use, the measurement approach is not feasible, as measurements are often impractical, time-consuming and expensive. Numerical modeling could be a more suitable means of predicting rainfall distributions. This was also indicated by Sharon and Arazi (1997), who stated that accurate measurements are in the first place a valuable tool for the verification of numerical models that can then be used as a predictive tool.

Only a few authors have employed numerical modeling. The first modeling efforts were made by Poreh and Mechrez (1984) and by Stout et al. (1993). These authors used analytical expressions for the wind field and numerical calculations of the raindrop motion. Bradley et al. (1997) used a simple potential flow model in combination with the calculation of raindrop trajectories to study the rainfall distribution over low hills (elevation up to 400 m). Up to now, full numerical studies – i.e. including

numerical modeling of the wind-flow field – have only been performed by Arazi et al. (1997) and by Choi (2002). These research efforts have all provided valuable information.

Despite the progress made, a lot of work remains to be done. To be useful in practice, the existing knowledge and calculation techniques should now be converted into a generalized numerical simulation model that is extended into the time domain. This model will allow the WDR distribution to be determined in both space and time, for any type of topography and for any type of rain event. Furthermore, a thorough understanding of the interaction between wind, rain and small-scale topography and of the resulting complex WDR distribution patterns – even for very simple topographical features – has not yet been attained. Also a detailed analysis of the importance of the different influencing parameters, such as type of topography, wind speed, raindrop diameter and rainfall intensity has not yet been performed. The main objective of this study is to develop such a model and to apply it to identify and explain the distinct distribution patterns for a simple 2D hill and 2D valley configuration. Specific attention will be paid to the numerical accuracy of the calculations (modeling choices and error analysis) and to the detailed and systematic investigation of the influencing parameters.

The model that is presented and applied is based on Computational Fluid Dynamics (CFD). It is important to note that confidence in using this type of model has been obtained earlier by the application and successful experimental validation of a similar model to obtain quantitative predictions of the WDR distribution on the vertical faces of bluff bodies (buildings) (Blocken and Carmeliet 2002, 2004).

The paper starts with providing some definitions and the influencing parameters of WDR. Next, the extended numerical model is developed and applied.

2. Definitions and parameters

Rainfall sum (S) is measured in L/m² or mm. Rainfall rate or intensity (R) is measured in L/m²h or mm/h. The rainfall sum or intensity measured by a conventional rain gauge with a horizontal orifice placed on level ground sufficiently far away from any obstructions and divided by the area A of the orifice, is termed reference meteorological rainfall (R or S) (Fig. 1a). The rainfall measured by a conventional rain gauge placed on sloping ground, divided by the area A, will generally differ from the reference meteorological rainfall due to the disturbance of the wind-flow pattern and the redistribution of rainfall by the local topography. It is called the meteorological rainfall (R_0 or S_0) (Fig. 1b). The rainfall measured by a tilted rain gauge with the orifice parallel to the ground surface, divided by the projected area of the rain gauge orifice ($A\cos\theta$), is called hydrological rainfall or hydrologically effective rainfall (R^* or S^*) (Fig. 1c). The latter generally differs from the meteorological rainfall because of two reasons: the inclined orifice and the division by the projected area. This study will focus on the hydrological rainfall sum S^* and on the hydrological rainfall intensity R^*. The acronym WDR (wind-driven rainfall) will refer to these quantities.

To quantify the WDR distribution, we introduce two dimensionless parameters: the specific catch ratio $\eta_d(d,t)$ and the catch ratio $\eta(t)$. The specific catch ratio is defined as the ratio of the hydrological rainfall intensity $R^*(d,t)$ and the reference meteorological rainfall intensity $R(d,t)$, both at time t and only composed of raindrops with diameter d. The catch ratio is defined in a similar way, but it relates to the entire spectrum of raindrop diameters: Eq. (1):

$$\eta_d(d,t) = \frac{R^*(d,t)}{R(d,t)} \quad , \quad \eta(t) = \frac{R^*(t)}{R(t)} \tag{1}$$

In practical applications, η_d and η will be calculated for discrete time steps $[t_n, t_n+\Delta t]$. The (specific) catch ratio for a discrete time step is redefined as:

$$\eta_d(d,t_n) = \frac{\int_{t_n}^{t_n+\Delta t} R^*(d,t)\,dt}{\int_{t_n}^{t_n+\Delta t} R(d,t)\,dt} = \frac{S^*(d,t_n)}{S(d,t_n)} \quad , \quad \eta(t_n) = \frac{\int_{t_n}^{t_n+\Delta t} R^*(t)\,dt}{\int_{t_n}^{t_n+\Delta t} R(t)\,dt} = \frac{S^*(t_n)}{S(t_n)} \tag{2}$$

where $S^*(d,t_n)$ and $S(d,t_n)$ are the hydrological rainfall sum and the reference meteorological rainfall sum for raindrops of diameter d during the time step. $S^*(t_n)$ and $S(t_n)$ refer to the same quantities but integrated over the entire spectrum of raindrop diameters. When η has been determined, the corresponding hydrological rainfall sum can be obtained by simply multiplying η with the reference meteorological rainfall sum.

The catch ratio η is a complicated function of space and time. The six basic influencing parameters for η as defined in Eq. (2) are: (1) geometry of the topographic feature (including the geometry of the surroundings), (2) position on the topography, (3) reference wind speed, (4) reference wind direction, (5) reference meteorological rainfall intensity and (6) horizontal raindrop-size distribution. The turbulent dispersion of raindrops will be neglected. Turbulent dispersion refers to the deviations in the motion of falling raindrops caused by turbulent wind gusts. This will be discussed later. The reference wind speed U (also indicated by U_{10}) (m/s) refers to the horizontal component of the wind velocity vector at 10 m height in the upstream-undisturbed airflow over flat topography. The reference wind direction (φ, in degrees from north) refers to the direction of the reference wind speed. The horizontal raindrop-size distribution $f_h(d)$ (m^{-1}) refers to the raindrop-size distribution as a flux through a horizontal plane, as opposed to the raindrop-size distribution in a volume of air (as it is usually specified).

3. Numerical model

The development of the numerical model starts from a steady-state simulation technique for raindrops in a wind field that is similar to the technique used by Arazi et al. (1997) and Choi (2002). This technique will be briefly outlined. Next, some important rain modeling issues that have been included in this study – and that are sometimes wrongfully neglected – will be discussed. Afterwards, the steady-state technique will be extended into the time domain. Finally, some important considerations about accuracy and reliability of the numerical model will be given.

3.1. Steady-state numerical simulation technique

The steady-state simulation technique consists of four steps:

(1) The steady-state wind-flow pattern over the topographic feature is calculated using a CFD code.

(2) Raindrop trajectories are obtained by injecting raindrops of different sizes in the calculated wind-flow pattern and by solving their equations of motion.

(3) The specific catch ratio η_d is determined based on the injection and end positions of the calculated raindrop trajectories.

(4) The catch ratio η is calculated from η_d and the size distribution of raindrops.

3.1.1. Steady-state wind-flow pattern

The steady-state wind-flow pattern is determined by a CFD code that solves the complex 2D or 3D Reynolds-Averaged Navier-Stokes (RANS) equations for an incompressible flow with constant viscosity. Closure is obtained by adopting a turbulence model. In the present study, the "realizable" k-ε model developed by Shih et al. (1995) is used. The numerical procedure is started by constructing a model of the topographic feature under study and a computational domain around it in which the flow field will be solved. The control volume technique is used. It consists of dividing the computational domain into a large number of discrete control volumes: the computational mesh. The governing equations (RANS and turbulence model equations) are then integrated for each control volume to obtain discretized algebraic equations. The latter equations express the conservation laws on a control volume basis and can be solved numerically. In the present paper, the equations are solved using second-order upwind discretization for the convection and diffusive terms. Pressure-velocity coupling is provided by the SIMPLE scheme. Pressure interpolation is performed with the standard scheme (Fluent Inc. 1998). The results of the calculation are the numerical values of the two (in 2D) or three (in 3D) wind speed components, pressure, k and ε at each control volume center point.

3.1.2. Raindrop trajectories

The raindrop trajectories are determined based on the calculated steady-state wind-flow pattern (velocity vectors $\vec{V}$). The equation of motion of a raindrop is:

$$\left(\frac{\rho_w - \rho}{\rho_w}\right)\vec{g} + \frac{3\mu}{\rho_w d^2}\cdot\frac{C_D\,Re}{4}\cdot\left(\vec{V} - \frac{d\vec{r}}{dt}\right) = \frac{d^2\vec{r}}{dt^2} \tag{3}$$

where Re is the relative Reynolds number (referring to the airflow around an individual raindrop):

$$Re = \frac{\rho d}{\mu}\left\| \vec{V} - \frac{d\vec{r}}{dt} \right\| \tag{4}$$

and ρ_w is the density of the raindrop, ρ the air density, g the gravitational constant, C_D the raindrop drag coefficient and $\vec{r}$ the position vector of the raindrop in the xyz-space. The raindrop trajectories can be calculated in a piecewise analytical manner (Blocken 2004). The raindrop drag coefficient will be discussed later.

3.1.3. Specific catch ratio

The calculation of the specific catch ratio η_d is performed by the following procedure. For simplicity, a 2D situation is assumed (Fig. 2). In a steady-state wind-flow pattern – thus neglecting turbulent dispersion of raindrops – two trajectories of raindrops with diameter d form a stream tube. Let $\overrightarrow{R_d}$ represent the rain intensity vector related to the raindrops of diameter d (L/m²h). The flux of this vector through the horizontal surface A_h that is situated outside the disturbed wind field is equal to the product of the reference meteorological rainfall intensity R(d) (L/m²h) and the surface area A_h. This volume of rainfall per hour (L/h) flows through the stream tube and falls on the sloping soil surface A_s. Conservation of mass for the raindrops in the stream tube allows η_d to be expressed in terms of areas:

$$\eta_d(d) = \frac{R^*(d)}{R(d)} = \frac{A_h}{A_s\cos\theta} \tag{5}$$

Here, $A_s\cos\theta$ is the horizontal projection of the slope area A_s that is bounded by the trajectory endpoints. In the simulation, it is important that the location of the plane A_h must allow the raindrops injected at that position to reach their terminal velocity of fall (vertical) and the wind velocity (horizontal) before entering the flow pattern disturbed by the topographic feature.

3.1.4. Catch ratio

The catch ratio η is obtained by multiplying η_d for each raindrop diameter d with the fraction of these drops in the rain (horizontal raindrop-size distribution $f_h(d)$) and integrating over all raindrop diameters:

$$\eta = \int_d f_h(d)\,\eta_d(d)\,d\,d \tag{6}$$

3.2. Rain modeling considerations

Drag coefficient formulae C_D for spherical particles (Morsi and Alexander 1972) are often used in raindrop trajectory calculations, as only these are available in many commercial CFD codes. As falling raindrops deviate from the spherical shape (Pruppacher and Klett 1978), these drag coefficients are an underestimation of the real ones, especially at high relative Reynolds numbers. Appropriate drag coefficients for falling raindrops were measured by e.g. Gunn and Kinzer (1949) and have been implemented in the particle tracking procedures written by the current authors.

As measuring raindrop-size distributions with good accuracy is difficult (Salles et al. 1999) and such data are not generally available, information on raindrop-size spectra must be obtained from empirical formulae. For the present study, the formula of Best (1950) is adopted. It is supported by a wide bibliographical survey and by measurements for a large number of rain events. His findings indicated that in many cases the size distribution of raindrops is in good accordance with Eq. (7):

$$F(d) = 1-\exp\left(-\left(\frac{d}{a}\right)^n\right) \quad , \quad a = A\,R^p \quad , \quad f(d) = \frac{d\,F}{d\,d} \tag{7}$$

where F(d) is the fraction of liquid water *in the air* with raindrops of diameter less than d and A, n, p are parameters the experimentally determined averages of which are 1.30, 2.25, 0.232 respectively. The function f(d) yields the probability density of drop size in a volume of air. Due to the variation of the terminal velocity of fall of a raindrop with size, the raindrop-size distribution *in a volume of air* differs from the raindrop-size distribution *as a flux through a horizontal plane*. The former can be converted to the latter by multiplying with the raindrop terminal velocity of fall $v_t(d)$:

$$f_h(d) = \frac{f(d)\,v_t(d)}{\int_d f(d)\,v_t(d)\,d\,d} \tag{8}$$

where $f_h(d)$ represents the raindrop-size distribution through a horizontal plane and f(d) the raindrop-size distribution in the air. The denominator is necessary to ensure that the area under the curve $f_h(d)$ vs. d remains equal to unity. Results of raindrop terminal velocity measurements can be found in e.g. Gunn and Kinzer (1949). $f_h(d)$ is presented in Fig. 3 for various reference rainfall intensities.

3.3. Numerical model for wind-driven rainfall distribution in space and time

3.3.1. Objective of the model extension into the time domain

Taking into account the rain modeling considerations described in section 3.2, the steady-state simulation technique (section 3.1) is incorporated into a generalized numerical simulation model. The objective of the numerical model is to predict both the spatial and temporal distribution of WDR over topographic features for transient (i.e. time-varying) rain events. A rain event is defined here as a period of time of variable length during which it rains at least once, and that can be interspersed with periods without rainfall. The spatial WDR distribution is obtained by determining the catch ratio η at each position on the topography. The temporal distribution results from performing these calculations for user-defined discrete time steps. The time scale at which the weather data samples are available is called the experimental time scale and the corresponding time step is noted as Δt^e (index i). The user-defined time scale at which the catch ratio is calculated is called the numerical time scale and the corresponding time step is noted as Δt^n (index j). The numerical time step is larger than or equal to the experimental time step and comprises an integer number of experimental time steps. The definitions of experimental and numerical time step are needed because the experimental data is usually high-resolution data, while the calculated results will often refer to larger time scales. The size of the numerical time step is determined by the application for which the calculated results will be used (e.g. water infiltration in soils: Δt^n = 1 hour or 1 day, Δt^e = 1 or 10 minutes). Fig. 4 represents a schematic of input and output data in the numerical model for Δt^e = 10 minutes and Δt^n = 1 hour.

3.3.2. Methodology

In the following, the discussion is limited to two dimensions. Recalling the six basic influencing parameters for the catch ratio η mentioned in section 2 and with wind direction dropping out in the 2D case, for a given topography and a given position on the topography, the catch ratio is a function of the reference wind speed U, the reference rainfall intensity R and the horizontal raindrop-size distribution $f_h(d)$. When the raindrop-size distribution of Best is adopted (Eq. 7 and 8), a unique relation exists between the reference rainfall intensity and the raindrop spectrum, causing the reference wind speed and rainfall intensity values to unambiguously define the catch ratio.

The steady-state simulation technique can be used to calculate the catch ratio under steady-state conditions, i.e. for fixed values of reference wind speed and rainfall intensity. To determine the catch ratio for a transient rain event, with fluctuating wind speed and rainfall intensity, this event is partitioned into a number of equidistant time steps, each of which is considered steady-state. The time step length is taken equal to the experimental time step size Δt^e (see Fig. 4). This way, with each time step (index i), a measured value of reference wind speed U_i (= U_{10}) and rainfall intensity R_i is associated. For each (experimental) time step i, the corresponding catch ratio can now be calculated by employing the steady-state technique for the couple (U_i, R_i).

To reduce the computational expense, the steady-state technique will only be employed for a limited number of reference wind speed and rainfall intensity couples (U_i, R_i), while intermediate results will be obtained by linear interpolation. A number of steady-state values for η are numerically calculated for particular positions on the topography and for various combinations of reference wind speed U (…U_k, U_i, U_{k+1}, …) and rainfall intensity R (… R_l, R_i, R_{l+1}, ...). With these values, catch ratio charts can be constructed as presented in Fig. 5a. Let us consider an experimental time step i in the rain event and let the corresponding couple (U_i, R_i) be situated in segment (k,l) as shown in Fig. 5a:

$$U_k \leq U_i < U_{k+1} \quad , \quad R_l \leq R_i < R_{l+1} \tag{9}$$

Each segment (k,l) is characterized by four calculated values for η (Fig. 5b). As these values generally do not define a plane in the (U, R, η) space, the segment is split up into two partial segments $(k,l)^{(1)}$ and $(k,l)^{(2)}$ (Fig. 5b). Each of these partial segments is characterized by three η-values that do define a plane. For each of these partial segments, this plane is used as an approximation for the actual surface $\eta = f(U, R)$. The value of the catch ratio η_i for each couple (U_i,R_i) is then extracted from the catch ratio chart by linear interpolation in these planes. Finally, the catch ratio for the numerical time step j (η_j) is determined from the catch ratios for each of the experimental time steps i (η_i) that are comprised in the time step j. This is done by expressing that the summed hydrological rainfall sum over all the time steps i comprised in the time step j must equal the hydrological rainfall sum for time step j:

$$\sum_i S_i^* = S_j^* \Leftrightarrow \sum_i \eta_i S_i = \eta_j \sum_i S_i \tag{10}$$

3.4. Accuracy and reliability

The accuracy and reliability of the numerical simulation model is mainly governed by two modeling choices: (1) the numerical discretization and (2) the turbulence model.

3.4.1. Numerical discretization

The numerical discretization error of the CFD calculation of the wind-flow field depends on the size of the computational mesh, on the schemes employed for the discretization of the governing equations and on the variable gradients in the flow field. Second-order-accurate schemes are used whenever possible. Sometimes however, the calculation process becomes unstable and first-order-accurate schemes (which are more stable) have to be used. In order to minimize discretization errors in the calculation of the wind-flow field, small control volume sizes should be used in regions where large flow gradients are expected, i.e. close to the surface of the topography and behind it, especially when flow separation and recirculation is expected to occur. The discretization error for the wind-flow field can be estimated by solving the same problem on several systematically refined meshes and by employing the formula proposed by Ferziger and Peric (1996) followed by Richardson extrapolation. Since the present paper focuses on the WDR distribution, we are primarily interested in the accuracy at which we can determine this distribution, rather than the wind-flow field. Therefore, a slightly different procedure can be followed. Several meshes with different mesh resolutions are made, including one very fine mesh. The construction of the meshes will be discussed later. To construct the very fine mesh, the length scale of the control volumes in the finest of the other meshes is reduced by 4, meaning a total reduction with a factor $4^2 = 16$ in two dimensions. The solution on the very fine mesh is considered as the reference solution, and the discretization error on each of the other meshes is estimated by comparing the catch ratio distribution obtained from that mesh with that from the reference solution. In section 4, the mesh that was finally chosen will be given as well as the corresponding estimate of the discretization error.

3.4.2. Turbulence model

The adequacy of a turbulence model to be used for specific flow types is typically determined by comparing the numerical results from this model with experimental data. For the present study, the realizable k-ε model has been chosen for the following reasons:

(1) The k-ε family of turbulence models is the most widely validated of all turbulence models and offers a good compromise between robustness, economy and accuracy.

(2) Flows over topographical features such as hills and valleys are often characterized by flow separation. The standard k-ε model is known to provide inferior performance in simulating separated flows. The realizable k-ε model has been validated for a wide range of flows including separated flows and has been found to perform substantially better than the standard k-ε model (Shih et al. 1995, Kim et al. 1997).

(3) Finally, and most importantly, the use of the realizable k-ε model has been found to yield accurate quantitative predictions of the WDR distribution on the vertical faces of bluff obstacles (buildings) (Blocken and Carmeliet 2002, 2004).

4. Application

4.1. Geometry

The model is applied to determine the WDR distribution over two sinusoidal topographic configurations: a 2D hill and a 2D valley. The geometry is defined by the following equation:

$$z = \pm \frac{H}{2}\left[1+\sin\left(\pi\frac{4x-L}{2L}\right)\right] \tag{11}$$

where the positive sign is used to describe the hill surface and the negative sign to describe the valley surface. The parameter L, hill or valley length, is 100 m. The height/depth H is 30 m. Fig. 6 illustrates the geometry.

4.2. Steady-state numerical simulations

Steady-state numerical simulations are conducted for a selected set of couples (U_i, R_i) to construct catch ratio charts for each position on the topography. The simulations comprise the calculation of the wind-flow pattern, the raindrop trajectories, the specific catch ratio and the catch ratio.

4.2.1. Wind-flow pattern

Models of both configurations are placed in a computational domain that is 1500 m long and 300 m high. The typology and size of the mesh is indicated in Fig. 7. The domain is meshed in identically the same way for the two configurations. It is divided into eight faces, each of which is meshed with triangular control volumes. The mesh size is increased from bottom to top of the domain. The configurations are placed in a boundary-layer flow with a power-law velocity inflow profile with exponent $\alpha = 0.15$, corresponding to smooth terrain (Eq. 12):

$$\frac{U(z)}{U_{10}} = \left(\frac{z}{10}\right)^{\alpha} \tag{12}$$

The roughness of the hill and valley surface is taken as 0.03 m, which corresponds to a surface covered with short grass. The computational domain is discretized with 83874 and 82288 control volumes for the hill and valley configuration respectively. The steady-state wind-flow pattern is calculated for reference wind speed U_{10} = 1, 2, 3, 4, 5, 6, 8, 10, 15, 20, 25 and 30 m/s. Wind-flow profiles (horizontal velocity component) at various positions in the domain are given in Fig. 8. Note that Fig. 8 represents only part of the computational domain. For the hill, a large increase in wind speed is observed near the crest. Flow separation just beyond the crest causes a large vortex (recirculating flow) in the lee. It clearly influences the flow for a considerable distance downstream of the hill. The valley modifies the wind flow only locally. Flow separation occurs at the upstream valley edge, causing a large recirculation vortex inside the valley. These features will have a significant influence on the raindrop trajectories and the (specific) catch ratio as will be shown in the next sections.

4.2.2. Raindrop trajectories

For each of the calculated wind-flow patterns, 2D Lagrangian particle tracking is performed for raindrops with 15 different diameters ranging from 0.5 to 1 mm in steps of 0.1 mm, from 1 to 2 mm in steps of 0.2 mm and from 2 to 6 mm in steps of 1 mm. Fig. 9 shows particle trajectories of 0.5, 1.0 and 6.0 mm drops in the 5 m/s flow fields. In general, it is seen that for smaller drops, the trajectories are more inclined and their distortion near the hill and in the valley is more pronounced. For larger drops (higher inertia), the trajectories are less inclined and more rectilinear. In particular, three observations are made: (1) for the hill configuration, not only the raindrop trajectories ending on the hill itself are influenced by it but also those ending a considerable distance upstream and especially downstream of the hill. This is not the case for the valley. This observation directly corresponds with the disturbance of the wind-flow pattern described in the previous section. (2) At the windward slope of the hill, the trajectories ending on the upper half are swept upwards, while the trajectories ending on the lower half are deflected downwards. (3) The recirculation vortex in the lee of the hill and inside the valley is responsible for the curvature of the raindrop trajectories in these regions. Note that, since the raindrops were injected equidistantly from a straight horizontal line, the density of the raindrop trajectory endpoints – measured along a horizontal line – on the hill and valley surface is a direct measure of the quantity of WDR (specific catch ratio).

4.2.3. Specific catch ratio

To obtain high-resolution information, arrays of 300 raindrop trajectories with a spacing of 1 m are injected from a straight horizontal line at a height of about 100 m above the topography. Based on these trajectories, η_d is obtained following the procedure outlined in section 3.1.3. This procedure is performed for each reference wind speed and each raindrop diameter. The spatial variation of η_d as a function of

reference wind speed and raindrop diameter is shown in Fig 10. The following observations are made (note that $\eta_d > 1$ on a certain position implies that the hydrological rainfall sum/intensity at that position is larger than the reference meteorological rainfall sum/intensity):

For the hill configuration:

(1) Fig. 10a1: Influence of wind speed on η_d: A distinct wetting pattern is found, and the gradients in this pattern become more pronounced as the wind speed increases. A first positive peak is present at the lower three quarters of the windward slope. The position of this peak value remains relatively fixed with increasing wind speed. Following this positive peak, a negative peak is observed that stretches from the upper part of the windward slope to the crest and a certain distance down the lee slope. It clearly gets wider as wind speed increases. Immediately following the negative peak is a second positive peak, the position of which is shifted downstream with higher wind speeds. It is noted that a value larger than unity is present even beyond 150 m, i.e. 50 m behind the leeward slope of the hill, due to the presence of the large recirculation vortex.

(2) Fig. 10b1: Influence of raindrop size on η_d: The first positive peak is most pronounced for the larger raindrops, whereas the opposite holds for the negative peak. The second positive peak vanishes for large raindrops.

For the valley configuration:

(1) Fig. 10a2: Influence of wind speed on η_d: The wetting pattern exhibits a negative peak just beyond the upstream valley edge and a positive peak of approximately the same magnitude at the upper half of the wind-facing slope. In contrast to the hill configuration, the positions of the positive and negative peaks are quite fixed. At a wind speed of 10 m/s and above, secondary peaks appear resulting in a more complicated wetting pattern.

(2) Fig. 10b2: Influence of raindrop size on η_d: The influence of raindrop size is most apparent for the larger drops: the maximum/minimum values are slightly increased and the positive and negative peaks are stretched more towards the center of the valley.

Zooming into two selected positions on the hill and on the valley slope, the dependency of η_d on reference wind speed and raindrop diameter can be represented with surface plots as shown in Fig. 11 and Fig. 12. These plots are specifically displayed to indicate the complexity of determining the WDR distribution, even on simple 2D geometries as are studied here. Note that the scaling on the vertical axis is different for each figure.

(1) Figure 11 (hill) illustrates the different behavior of η_d at two positions on the windward slope. At 25 m, i.e. at half the slope height, η_d increases approximately linearly with wind speed from 1.0 to about 2.5. An increase with raindrop diameter is observed, but only for the smaller drops (d = 0.5 – 2.0 mm). At 42 m, near the crest, η_d increases slightly with wind speed for values below 10 m/s (from 1.0 to about 1.2). Above 10 m/s, it decreases and the decrease is most pronounced for the

smaller drops. The reason is that the drops tend to be blown over the crest as the wind speed increases and the raindrop diameter decreases.

(2) Figure 12 (valley) displays η_d at positions just beyond the upstream valley edge (10 m) and at half the height of the downstream slope (75 m). Note that it was necessary to invert the direction of the horizontal axes in the left figure in order to clearly illustrate the surface plot. At x = 10 m, η_d decreases with increasing wind speed (from 1.0 to 0.3), and the behavior is quite similar for all drop sizes. The reason is again that the drops tend to be blown over this position. At x = 75 m, an increase with wind speed is found with a significantly different behavior for different drops (η_d ranges from 1.0 to 1.6 for the largest drops).

4.2.4. Catch ratio

The catch ratio η is obtained by integrating η_d over the raindrop spectrum (Eq. 6). This calculation is performed for each of the 13 wind speed values (U_{10} = 0 m/s up to 30 m/s) and for 19 reference rainfall intensity values (R = 0, 0.1, 0.5, 1, 2, 3, 4, 5, 6, 8, 10, 15, 20, 25, 30, 40, 50, 60, 80 mm/h).

Fig. 13 shows the resulting η-profiles for a limited number of reference wind speed and rainfall intensity values. The wetting pattern exhibits the same features as explained in the previous section. Wind speed clearly is the most important variable. The overall influence of rainfall intensity appears to be rather small for most positions.

Finally, Fig. 14 and 15 provide the charts for η: the catch ratio charts. The important influence of wind speed and the lesser influence of rainfall intensity are confirmed. Charts like these were generated for a large number of positions along the topography and the corresponding values for η were digitally stored as matrices during the calculation process. These charts and matrices constitute the information that is necessary to perform the simulations of the WDR distribution in time and space for time-varying rain events, as will be shown in section 4.3.

4.2.5. Discretization error

This section applies to the discretization error (and hence the numerical accuracy) of the calculation results shown above. From the numerical simulations of raindrops in wind fields it has appeared that the combination of high wind speed and small drops is most difficult to simulate, as especially the small drops are sensitive to small deviations (and hence also errors) in wind speed. Larger drops, with more inertia, are less sensitive. Therefore, estimates of the discretization error for the catch ratio calculation were determined for the most critical conditions: the highest wind speed (U_{10} = 30 m/s) and the lowest rainfall intensity (R = 0.1 mm/h, i.e. a large fraction of small drops in the rain, see Fig. 3). Additionally, discretization errors were also determined for R = 1 mm/h and 10 mm/h to demonstrate the decreased

sensitivity of large raindrops to wind speed deviations. The discretization errors were calculated as follows: at every data point along the transect, the absolute value was obtained of the difference between the η-value obtained from the very fine mesh and the η-value obtained from the mesh that was used for the simulations in the previous sections. These absolute values were summed for all data points and divided by the number of points, providing a measure of the average error. The very fine mesh consisted of over 10^6 control volumes and was constructed in the same way as the other meshes (see Fig. 7) but with a four times smaller control volume length scale. For the hill, the resulting errors were 5.7%, 5.1%, 3.7 % and for the valley: 6.0%, 3.0%, 2.5% for R = 0.1, 1, 10 mm/h respectively. The larger part of these errors is due to small shifts of the negative and/or positive peak values, resulting in large differences at the data points (topographic positions) near the peaks. Anyway, the errors were considered small and given the fact that the most critical conditions were examined, the selected meshes were considered fit for purpose.

4.3. Wind-driven rainfall distribution in time and space

4.3.1. Rain event

The numerical model is applied to determine the WDR distribution in time and space for an example rain event. The record of reference wind speed and rainfall intensity is given in Fig. 16a. The rain event is characterized by a period of low wind speed followed by a period of relatively high wind speed values. During each of these periods, a number of rain spells with small to moderate intensity occur. The total volume of reference meteorological rainfall that was collected at the end of the rain event is 41 mm. The procedure described in section 3.3 is now followed to determine the WDR distribution in time and space. The experimental time step is 10 minutes (measurement interval), the numerical time step is – arbitrarily – also taken as 10 minutes.

4.3.2. Wind-driven rainfall distribution in time

Fig. 16b illustrates the distribution of the cumulative WDR sum (hydrological rainfall) together with the cumulative reference meteorological rainfall sum during the rain event, at the positions 25 m and 42 m for the hill and the positions 10 m and 75 m for the valley. The positions themselves are illustrated in Fig. 14 and 15. The specific features of the time distribution can be studied by combining Fig. 14 and 15 with Fig. 16. It is clear that the largest differences in 10-minute hydrological rainfall sum for the different positions occur during the co-occurrence of high wind speed values and peak rainfall intensity values. In the first 300 time steps (3000 minutes), wind speed is low and differences are too. The reason is that for low wind speed values, η is about 1.0 for all positions (see Fig. 14 and 15). The differences significantly increase with increasing wind speed (time step 340 and following). The cumulative hydrological rainfall

sum at hill position 42 and the cumulative reference rainfall sum coincide most of the time. The reason is that the positive and negative differences between η and unity (see Fig. 14b) average out for the rain event considered.

4.3.3. Wind-driven rainfall distribution in space

The spatial distribution of the WDR sum at the end of the rain event is given in Fig. 17. The dashed horizontal line indicates the total reference meteorological rainfall sum (41 mm). The wetting patterns clearly exhibit the same features as discussed before. Very large differences in total hydrological rainfall sum are found along the topography. The difference between maximum and minimum amount on the hill is 92% of the reference rainfall sum. For the valley this value is 71%.

5. Discussion

- The application of the model in this paper has focused on the WDR distribution over two 2D, simple and theoretical topographic configurations, as a first step towards more complex simulations. It is important to note that the developed model can be applied for any type of small-scale topography, in two as well as in three dimensions. The extension of the model itself to three dimensions is straightforward: solving the 3D RANS equations and adding the wind direction as a variable in the catch ratio charts and in the interpolation procedure. However, accurate 3D CFD modeling of WDR over complex topography will require considerably larger computing resources and computing time. It is an important subject of future research.
- In performing the numerical simulations, efforts have been made to limit errors: the adequacy of the resolution of the mesh has been verified (discretization error) and a suitable turbulence model was selected based on earlier experimental verification and validation studies of WDR. Nevertheless, a number of assumptions have been made that can introduce some error:
  (1) A first assumption is adopting the raindrop-size distribution of Best. Although this formula is based on an extensive study for a large number of rain events, deviations from the prescribed spectra are likely to occur. However, the influence of drop size and of reference rainfall intensity (and hence of raindrop-size distribution) on the WDR distribution has been found to be relatively small in the above simulations. Furthermore, in earlier modeling work on WDR, using the spectrum of Best has been shown to provide accurate quantitative simulation results (Blocken and Carmeliet 2002, 2004). Although both remarks indicate that the influence of the choice of the raindrop spectrum is small, further research efforts are needed to systematically investigate the sensitivity of the numerical prediction to changes in raindrop-size distribution.
  (2) The presented numerical model does not take into account the turbulent dispersion of raindrops in the wind field. Experimental verification efforts of a similar numerical model for the case of

the vertical faces of a low-rise bluff obstacle (building) have indicated that turbulent dispersion can be neglected (Blocken and Carmeliet 2002, 2004). Nevertheless, this statement should be verified for the more general case of random topographical configurations.

(3) In the application of this study, 10-minute weather data was used as input. The natural fluctuations of wind and rain characteristics (see Fig. 16a) might suggest that measurements on a shorter experimental time scale are needed. On the other hand, meteorological data are often only made available on an hourly or daily basis. A study investigating the errors associated with the choice of the experimental time step is necessary.

- The entire procedure as outlined in this paper might seem time-consuming. However it is important to note that this is only the case for the construction of the catch ratio charts (more specifically, the CFD wind-flow simulations take more than 90% of the time – in 3D this percentage will be even higher). The set of steady-state simulations conducted for the present paper has taken 7 days on a workstation with 2 processors of 2 GHz and 3 Gbyte RAM, only 2 Gbyte of which has been used. The most time-consuming part (4 days) was performing a selected number of additional calculations on the very fine mesh to examine the discretization error. Without this, the entire set of simulations would have been finished within 3 days. Once the catch ratio charts are constructed for a given topography, predicting the spatial and temporal WDR distribution for any rain event takes only a few minutes.

6. Conclusions

- A numerical simulation model has been presented as a tool that can be used in hydrological studies. It predicts the WDR (wind-driven rainfall) distribution over small-scale topography in space and time. The model consists of setting up of catch ratio charts to be used in combination with standard meteorological data (reference wind speed, reference wind direction, reference meteorological rainfall intensity). The charts are constructed by conducting a set of steady-state numerical simulations of wind-flow and rainfall distribution. These simulations are the most time-consuming part of the model. Once the construction of the charts has been completed for a given topography, the WDR distribution for any rain event and at any time can be quickly numerically predicted. The results can be used for studies of catchment hydrology, for runoff and erosion studies and for the design of rainfall monitoring networks, for example.
- Confidence in using this type of model in hydrological studies has been obtained earlier by the use and successful validation of a similar model to obtain quantitative predictions of the WDR distribution on the vertical faces of bluff bodies (buildings) (Blocken and Carmeliet 2002, 2004).
- The model has been applied for two sinusoidal topographies: a 2D hill and a 2D valley. An error analysis has been performed to select an appropriate numerical mesh. The numerical simulation of WDR over the hill and valley has revealed the relationship between the wind-flow pattern, the raindrop diameter, the rainfall intensity and the WDR distribution pattern. The most important

influencing parameters are the geometry of the topography and the wind speed. The influence of rainfall intensity on the catch ratio charts is less important.

- Further research efforts will concentrate on examining the importance of the assumptions mentioned in section 5, on the study of the WDR distribution over different and more complex topographical configurations and on the experimental verification of the predicted distribution patterns.

Acknowledgements

The first author is a post-doctoral research fellow of the FWO-Flanders (Belgium). The FWO-Flanders (Research Fund) supports and stimulates fundamental research in Flanders. Their contribution is gratefully acknowledged.

Nomenclature

A	area of rain gauge orifice (m^2)
A_h	area of horizontal plane at a certain height in the unobstructed airflow (m^2)
A_s	area on sloping soil surface bounded by trajectory endpoints (m^2).
A, n, p	constants in drop-size distribution equation (-)
C_D	drag coefficient (-)
d	raindrop diameter (mm)
$F(d)$	fraction of liquid water in the air with raindrops of diameter less than d (-)
f	probability density of drop size in the air (m^{-1})
f_h	probability density of drop size through a horizontal plane (m^{-1})
H	height of hill / depth of valley (m)
i, j	number of experimental / numerical time step
k, l	segment numbers
k	turbulent kinetic energy (m^2s^{-2})
L	hill / valley length (m)
$\vec{r}$	position vector in xyz-space (m)
R	reference meteorological rainfall intensity (level terrain) (mm/h or L/m^2h)
R_0	meteorological rainfall intensity (unlevel terrain) (mm/h or L/m^2h)
R^*	hydrological rainfall intensity (unlevel terrain) (mm/h or L/m^2h)
$\overrightarrow{R_d}$	rainfall intensity vector related to raindrop diameter d (mm/h or L/m^2h)
Re	Reynolds number (-)
S	reference meteorological rainfall sum (level terrain) (mm or L/m^2)
S_0	meteorological rainfall sum (unlevel terrain) (mm or L/m^2)
S^*	hydrological rainfall sum (unlevel terrain) (mm or L/m^2)
t	time (s)
U	horizontal component of mean wind speed (ms^{-1})
U_{10}	reference wind speed (upstream hor. wind velocity component at 10 m height) (ms^{-1})

v_t	raindrop terminal velocity of fall (ms^{-1})
x, z	length and height co-ordinate (m)
α	power law exponent (-)
γ	angle of raindrop trajectory (°)
ε	turbulence dissipation rate (m^2s^{-3})
θ	slope angle (°)
Δt	time interval (s)
η_d, η	specific catch ratio, catch ratio (-)
μ	molecular dynamic viscosity ($kgm^{-1}s^{-1}$)
φ	reference wind direction (direction of reference wind speed) (° from north)
ρ, ρ_w	air density, water density (kgm^{-3})

References

1. Arazi, A., Sharon, D., Khain, A., Huss, A., Mahrer, Y. 1997. The windfield and rainfall distribution induced within a small valley: field observations and 2-D numerical modeling. Bound-Layer Meteorology 83, 349-374.
2. Barrow, A.P., Lettenmeier, D.P. 1994. Dynamic modeling of orographically-induced precipitation. Rev. Geophys. 32, 265-284.
3. Basist, A., Bell, G.D., Meentemeyer, V. 1994. Statistical relationships between topography and precipitation patterns. Journal of Climate 7(9), 1305-1315.
4. Best, A.C. 1950. The size distribution of raindrops. Quarterly Journal of the Royal Meteorological Society 76, 16-36.
5. Blocken, B. 2004. Wind-driven rain on buildings: measurements, numerical modelling and applications. Ph.D. thesis, Laboratory of Building Physics, Department of Civil Engineering, Katholieke Universiteit Leuven, 323 p.
6. Blocken, B., Carmeliet, J. 2002. Spatial and temporal distribution of driving rain on a low-rise building. Wind and Structures 5(5), 441-462.
7. Blocken, B., Carmeliet, J. 2004. A review of wind-driven rain research in building science. Journal of Wind Engineering and Industrial Aerodynamics 92(13), 1079-1130.
8. Bradley, S.G., Gray, W.R., Pigott, L.D., Seed, A.W., Stow, C.D., Austin, G.L. 1997. Rainfall redistribution over low hills due to flow perturbation. Journal of Hydrology 202, 33-47.
9. Choi, E.C.C. 2002. Modelling of wind-driven rain and its soil detachment effect on hill slopes. Journal of Wind Engineering and Industrial Aerodynamics 90 (9), 1081-1097.
10. Craig, D. 1980. Two examples of the effect of topography on rainfall distribution patterns. Weather 35(10), 301-307.
11. De Lima, J.L.M.P. 1990. The effect of oblique rain on inclined surfaces: a nomograph for the rain-gauge correction factor. Journal of Hydrology 115, 407-412.
12. Erpul, G., Norton, L.D., Gabriëls, D. 2002. Raindrop-induced and wind-driven soil particle transport. Catena 47(3), 227-243.
13. Erpul, G., Norton, L.D., Gabriëls, D. 2003. Sediment transport from interril areas under wind-driven rain. Journal of Hydrology 276(1-4), 184-197.
14. Ferziger, J.H., Peric, M. 1996. Computational methods for fluid dynamics. Springer Berlin, 356p.
15. Fluent Inc. 1998. Fluent 5 User's manual.
16. Fourcade, H.G. 1942. Some notes on the effects of the incidence of rain on the distribution of rainfall over the surface of unlevel ground. Transactions of the Royal Society of South-Africa 29(3), 235-254.
17. Geiger, R. 1965. The climate near the ground, Harvard University Press, Cambridge, 611 p.
18. Goossens, D., Poesen, J., Gross, J., Spaan, W. 2000. Splash drift on light sandy soils: a field experiment. Agronomie 20, 271-282.
19. Gunn, R., Kinzer, G.D. 1949. The terminal velocity of fall for water droplets in stagnant air. Journal of Meteorology 6, 243-248.
20. Haiden, T., Kerschbaum, M., Kahlig, P., Noblis, F. 1992. A refined model of the influence of orography on the mesoscale distribution of extreme precipitation. Hydrological Sciences Journal 37, 417-427.

21. Hamilton, E.L. 1954. Rainfall sampling on rugged terrain. Tech. Bull. U.S. Dep. Agric., No. 1096, 41p.
22. Hovind, E.L. 1965. Precipitation distribution around a windy mountain peak. Journal of Geophysical Research 70(14), 3271-3278.
23. Hutchinson, P. 1970. A contribution to the problem of spacing raingages in rugged terrain. Journal of Hydrology 12, 1-14.
24. James, J.W. 1964. The effect of wind on precipitation catch over a small hill. Journal of Geophysical Research 69(12), 2521-2524.
25. Kim, S.-E., Choudhury, D., Patel, B. 1997. Computations of complex turbulent flows using the commercial code FLUENT, in: Proceedings of the ICASE/LaRC/AFOSR Symposium on Modeling Complex Turbulent Flows, Hampton, Virginia.
26. Lentz, R.D., Dowdy, R.H., Rust, R.H. 1995. Measuring wind and low-relief topographic effects on rainfall distribution. Applied Engineering in Agriculture 11(2), 241-248.
27. Morsi, S.A., Alexander, A.J. 1972. An investigation of particle trajectories in two-phase flow systems, Journal of Fluid Mechanics 55(2), 193-208.
28. Poesen, J. 1985. An improved splash transport model. Zeitschrift fur Geomorphologie Neue Folge 29(2), 193-211.
29. Poesen, J. 1986. Field measurements of splash erosion to validate a splash transport model. Zeitschrift fur Geomorphologie Neue Folge, Suppl.-Band 58, 81-91.
30. Poesen, J. 1988. Surface sealing on sandy and loamy soils: some aspects of seal formation and the influence of sealing on water erosion subprocesses. Quaderni di Scienza del Suolo 1, 9-20.
31. Poreh, M., Mechrez, E. 1984. The combined effect of wind and topography on rainfall distribution. Journal of Hydrology 72: 1-23.
32. Pruppacher, H., Klett, J. 1978. Microphysics of clouds and precipitation, D. Reidel, Boston.
33. Reid, I. 1973. The influence of slope aspect on precipitation receipt. Weather 28, 490-494.
34. Salles, C., Poesen, J., Borselli, L. 1999. Measurement of simulated drop size distribution with an optical spectro pluviometer: sample size considerations. Earth Surface Processes and Landforms 24(6), 545-556.
35. Sandsborg, J. 1970. The effect of wind on the precipitation distribution over a hillock. Nordic Hydrology 4, 235-244.
36. Sharon, D., Arazi, A. 1997. The distribution of wind-driven rainfall in a small valley: an empirical basis for numerical model verification. Journal of Hydrology 201, 21-48.
37. Sharon, D., Morin, J., Moshe, Y. 1988. Micro-topographical variations of rainfall incident on ridges of a cultivated field. Transactions of the ASAE 31(6), 1715-1722.
38. Sharon, D. 1970. Topography-conditioned variations in rainfall as related to the runoff-contributing areas in a small watershed. Israel Journal of Earth Sciences 19, 85-89.
39. Sharon, D. 1980. The distribution of hydrologically effective rainfall incident on sloping ground. Journal of Hydrology 46, 165-188.
40. Sharon, D. 1983. Observations on the differential hydrological and/or erosional response of opposite-lying slopes, as related to incident rainfall. Israel Journal of Earth Sciences 32: 71-74.
41. Shih, T.-H., Liou, W.W., Shabbir, A., Zhu, J. 1995. A new k-e eddy-viscosity model for high Reynolds number turbulent flows – model development and validation, Computers and Fluids 24(3), 227-238.
42. Stout, J.E., Lin, Y.L., Arya, S.P.S. 1993. A theoretical investigation of the effects of sinusoidal topography on particle deposition. Journal of the Atmospheric Sciences 50, (15) 2533-2541

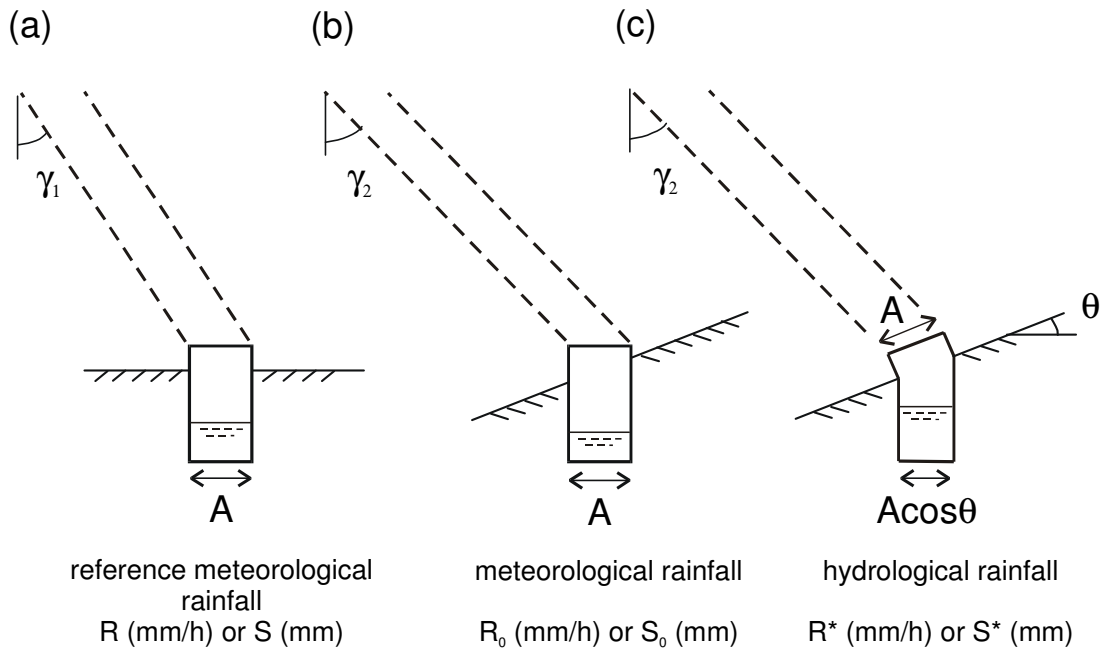

Fig. 1. Definition of (a) reference meteorological rainfall, (b) meteorological rainfall and (c) hydrological rainfall. R = rainfall rate, S = rainfall sum. γ_1 is the angle of the raindrop trajectories in an airflow over flat topography, far away from any obstructions. γ_2 is a local trajectory angle that is different from γ_1 because of the disturbance of the local airflow by the topographic relief.

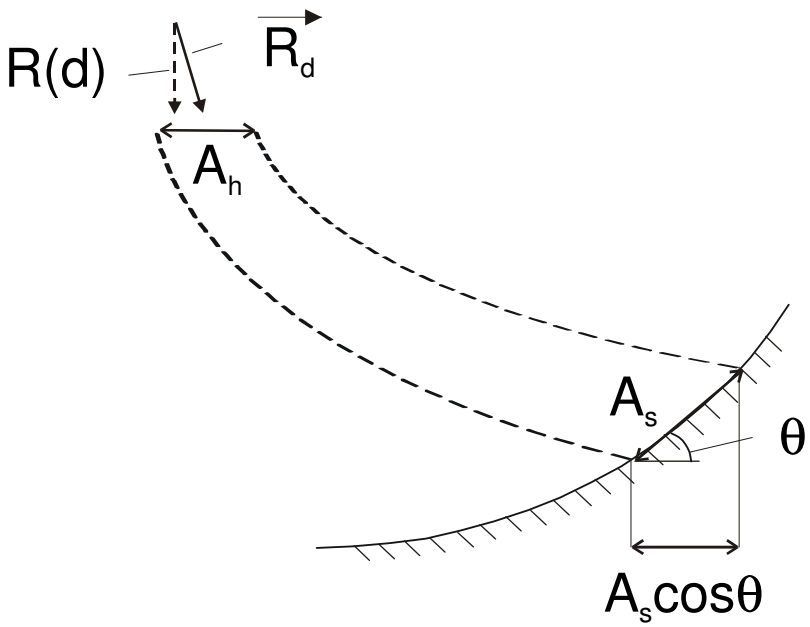

Fig. 2. Sketch illustrating the stream tube bounded by raindrop trajectories. Definition of the specific catch ratio η_d for raindrops with diameter d based on conservation of mass for the raindrops in the stream tube. The vector $\overrightarrow{R_d}$ is the rain intensity vector. Its flux through the surface A_h is $R(d).A_h$. This flux through the stream tube falls on the sloping soil surface A_s.

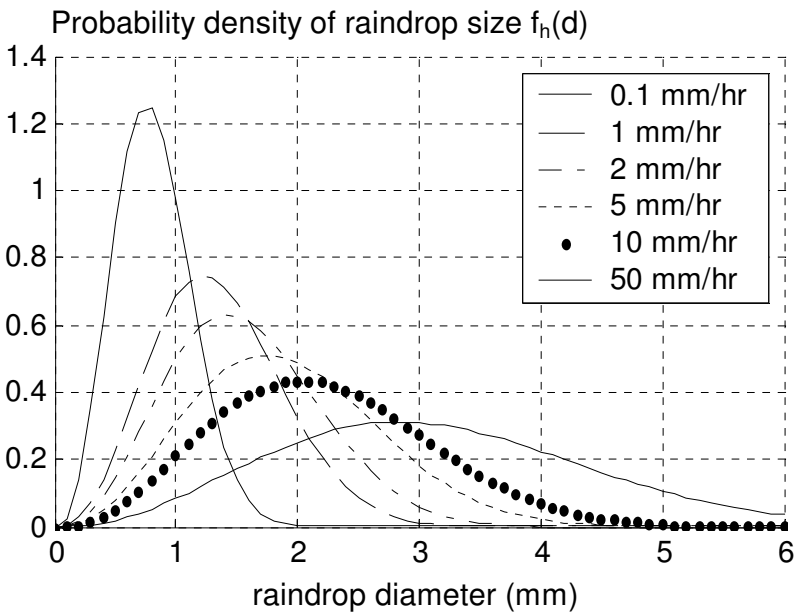

Fig. 3. Raindrop-size distribution $f_h(d)$ through a horizontal plane with the reference rainfall intensity as a parameter – calculated from the raindrop-size distribution in the air according to Best (1950).

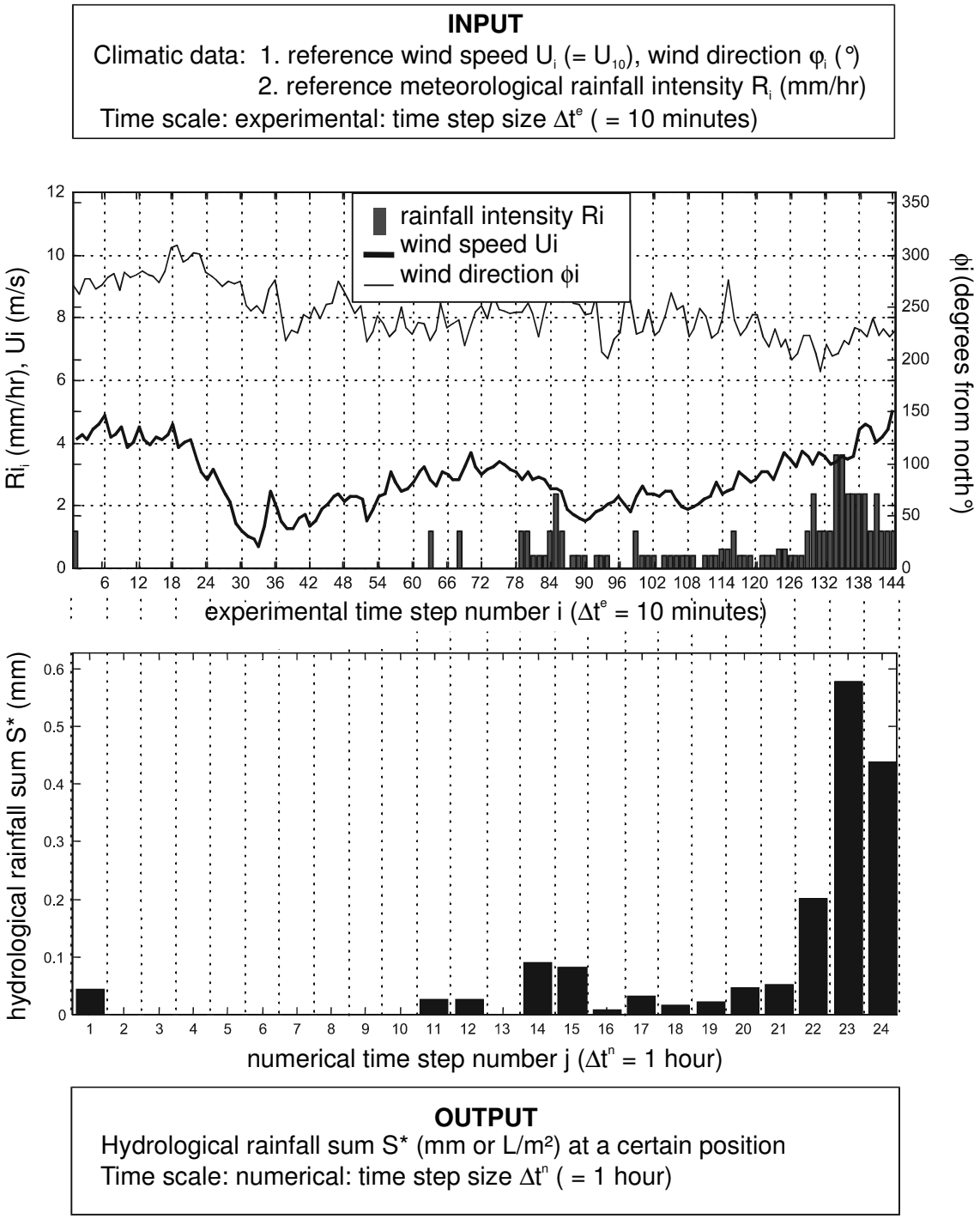

Fig. 4. Schematic representation of input and output data in the numerical simulation model for a fictitious situation.

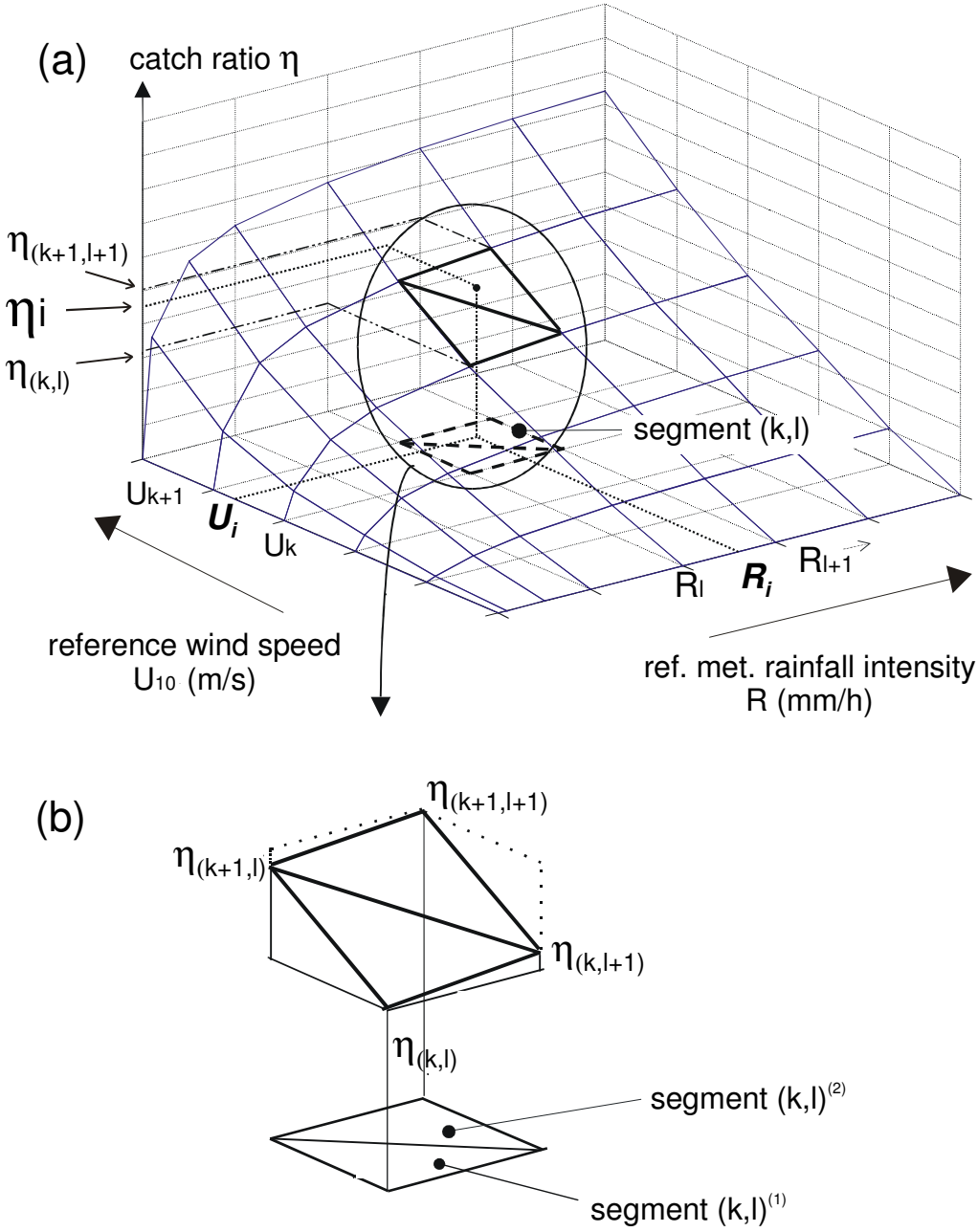

Fig. 5. (a) Example of a catch ratio chart giving the catch ratio η for a given position on the topography as a function of discrete values of reference wind speed U_{10} and reference meteorological rainfall intensity R. (b) Intermediate values are obtained by linear interpolation in triangular planes.

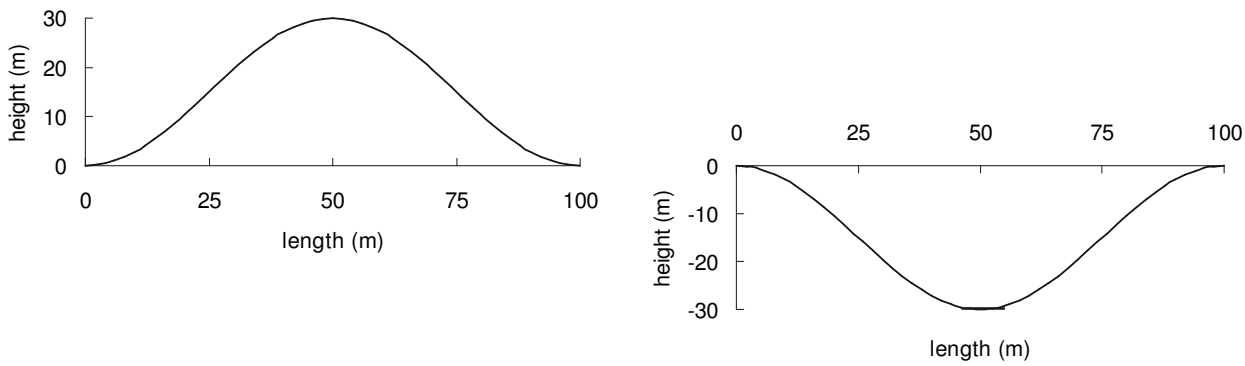

Fig. 6. Geometry and dimensions of the 2D sinusoidal hill and valley configuration.

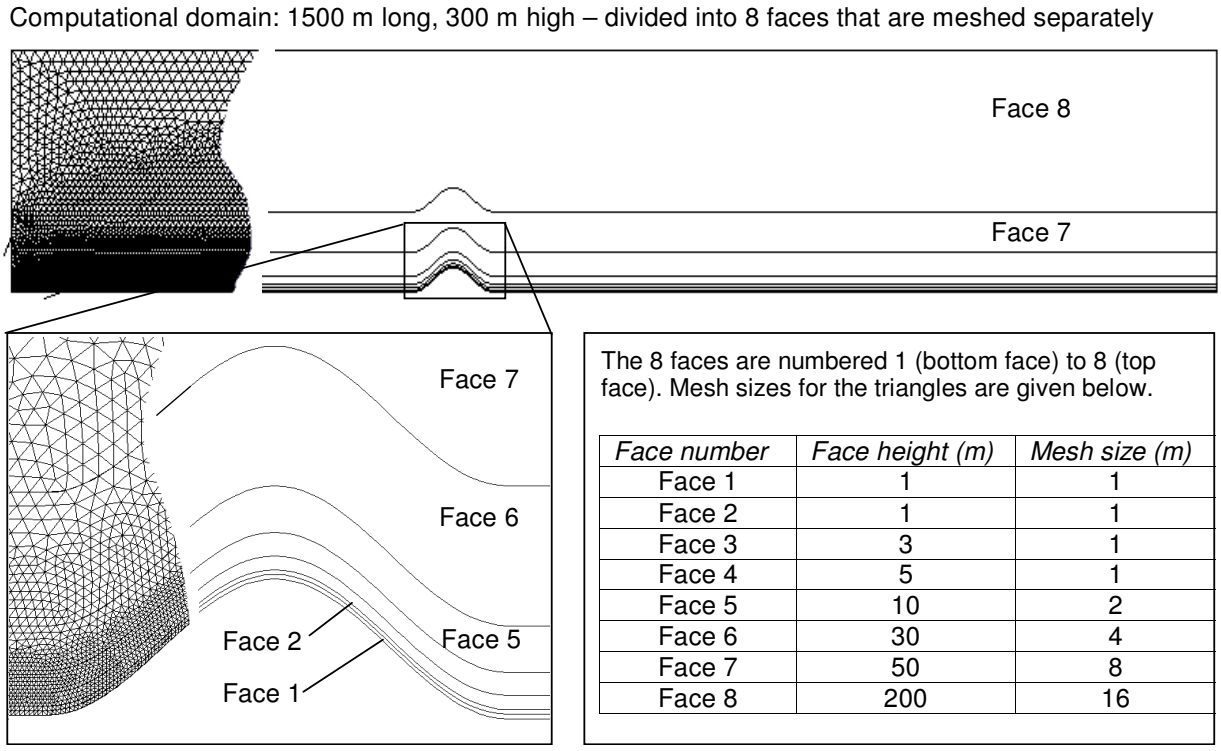

The 8 faces are numbered 1 (bottom face) to 8 (top face). Mesh sizes for the triangles are given below.

Face number	*Face height (m)*	*Mesh size (m)*
Face 1	1	1
Face 2	1	1
Face 3	3	1
Face 4	5	1
Face 5	10	2
Face 6	30	4
Face 7	50	8
Face 8	200	16

Fig. 7. Construction of the mesh. The computational domain (1500 m by 300 m) is divided into eight faces, each of which is meshed separately with triangular control volumes. The size of the control volumes is increased from bottom to top of the domain.

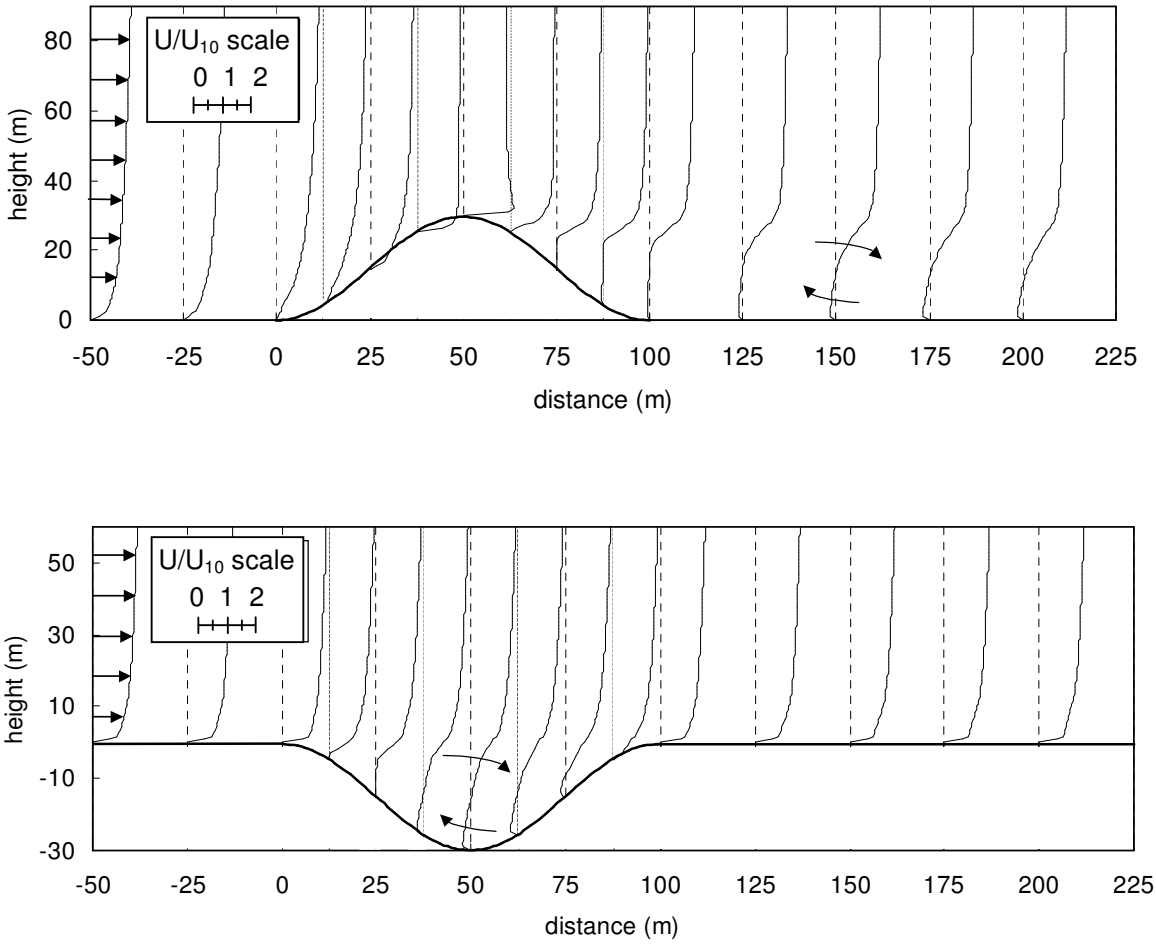

Fig. 8. Wind-flow profiles (ratio of horizontal velocity component U to reference wind speed U_{10} – i.e. the wind speed at a height of 10 m in the upstream undisturbed flow) at various positions in the domain. Top: flow over hill, bottom: flow over valley.

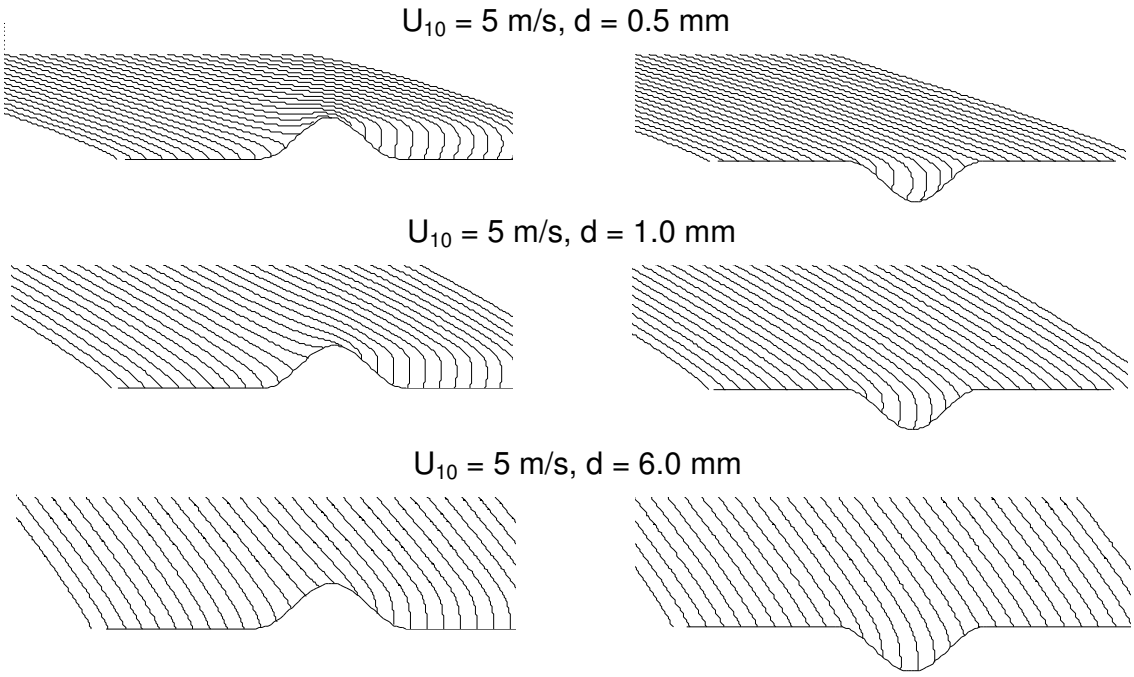

Fig. 9. Raindrop trajectories of drops with diameters 0.5, 1.0 and 6.0 mm in the U_{10} = 5 m/s wind-flow field.

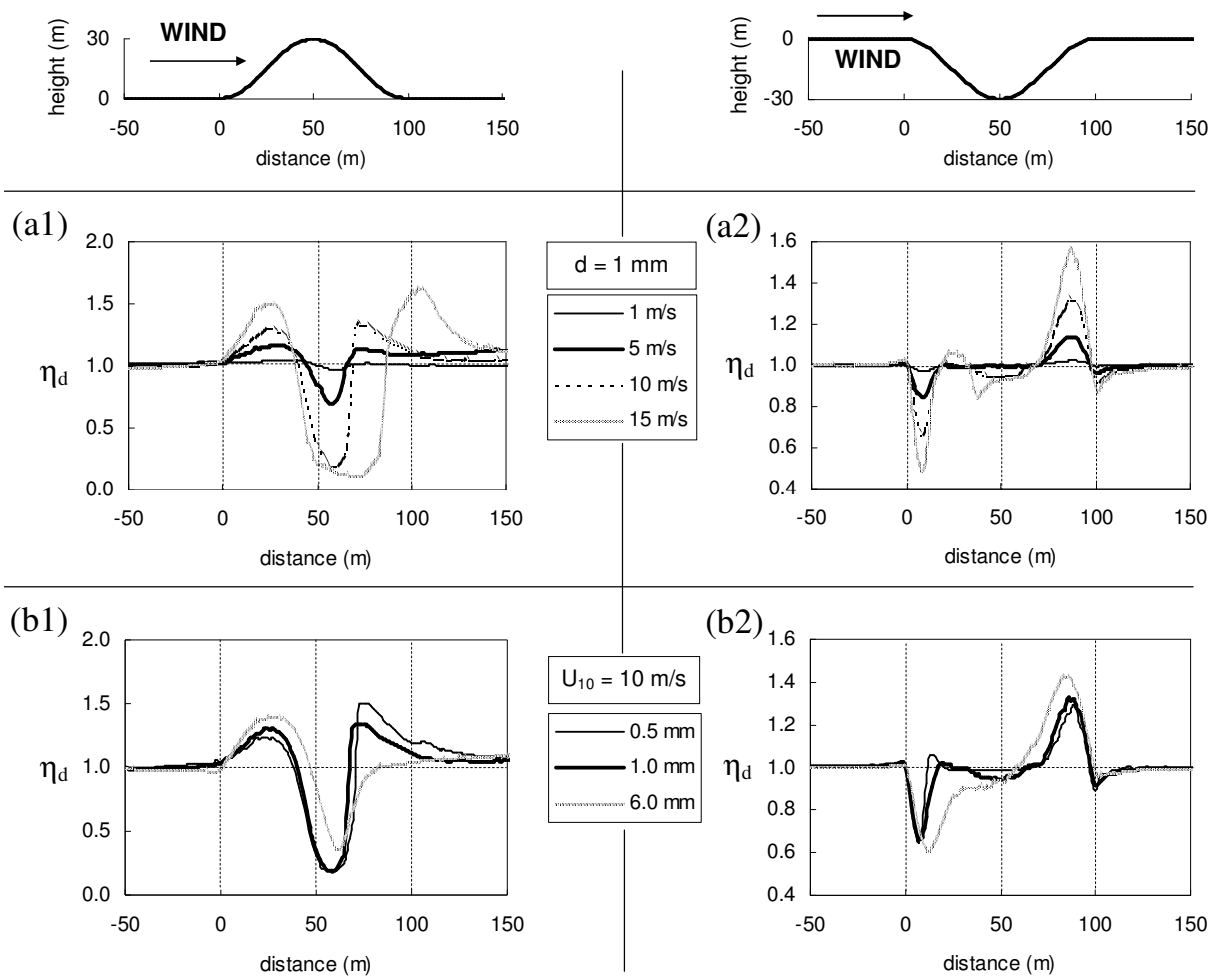

Fig. 10. Profiles of the specific catch ratio η_d along the hill and valley surface for (a) raindrop diameter d = 1 mm and different values of reference wind speed; (b) for reference wind speed U_{10} = 10 m/s and different values of raindrop diameter.

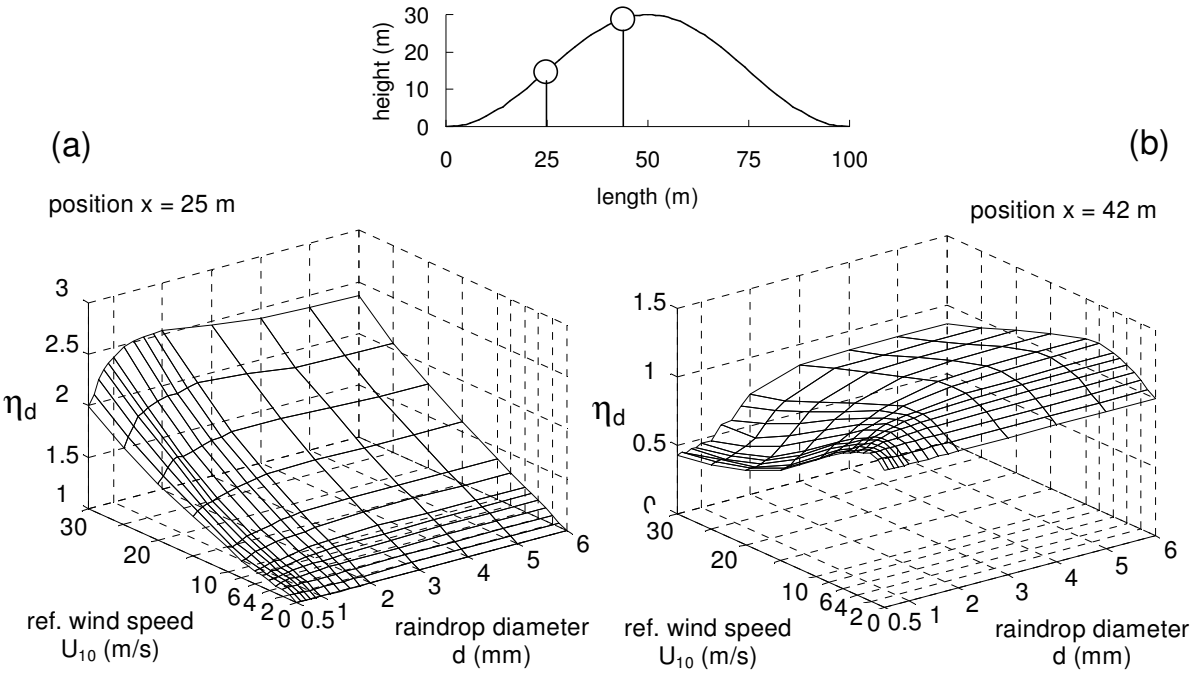

Fig. 11. Specific catch ratio η_d as a function of reference wind speed U_{10} and raindrop diameter d for (a) position x = 25 m and (b) position x = 42 m on the hill surface.

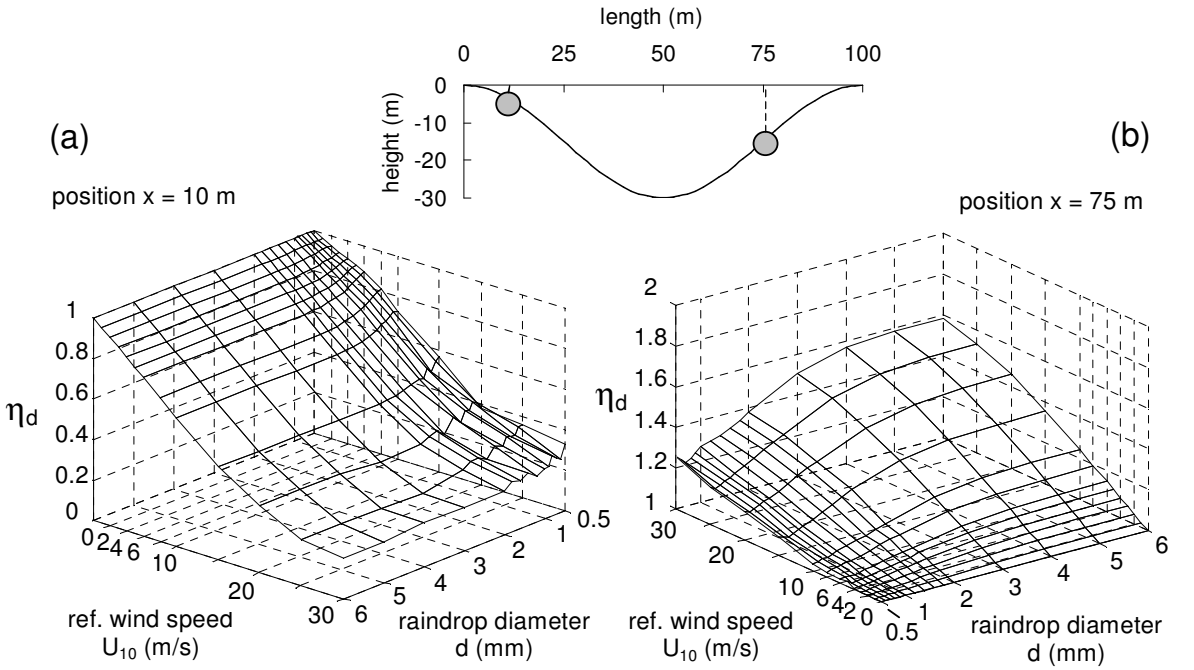

Fig. 12. Specific catch ratio η_d as a function of reference wind speed U_{10} and raindrop diameter d for (a) position x = 10 m and (b) position x = 75 m on the valley surface.

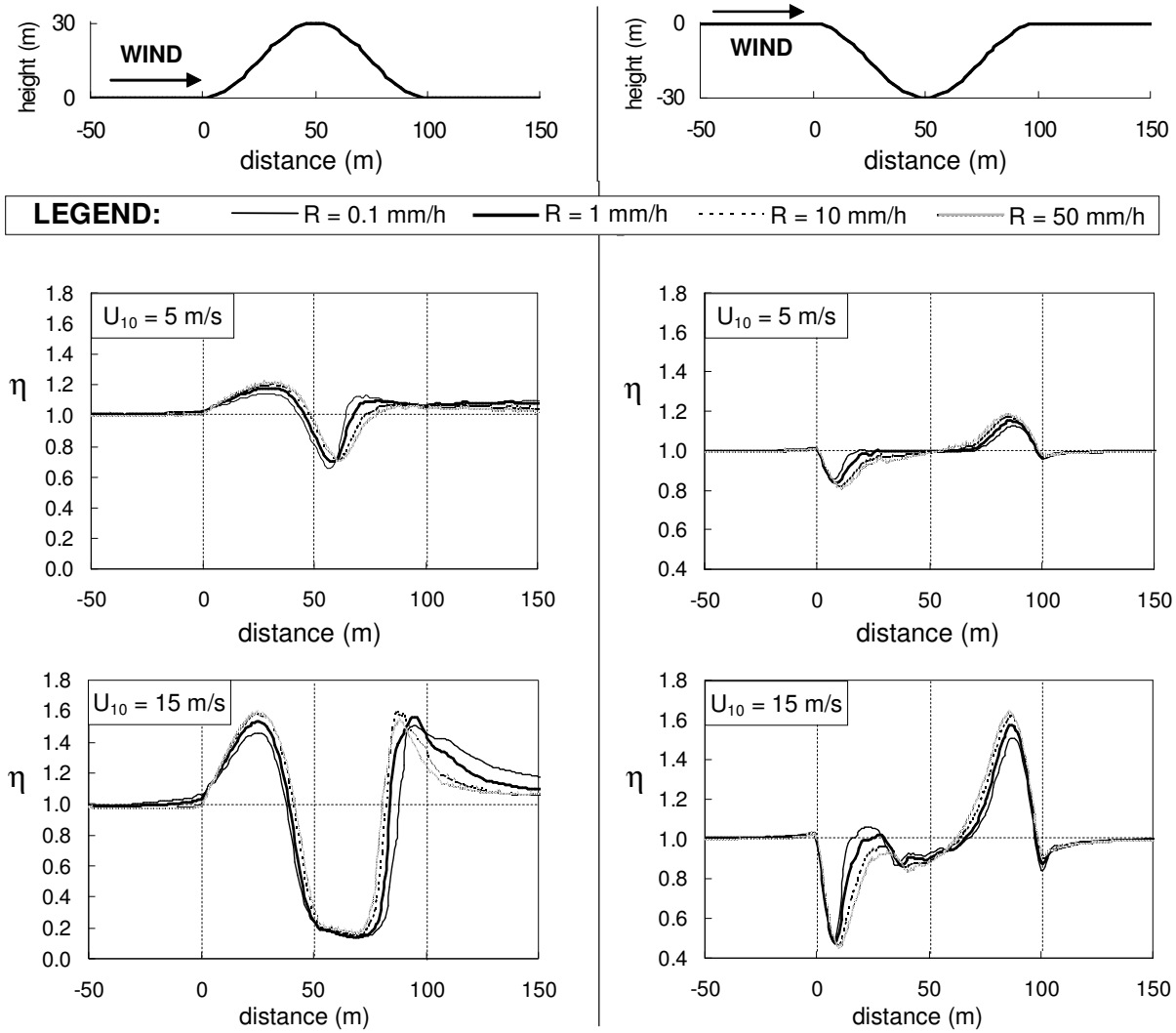

Fig. 13. Profiles of the catch ratio η along the hill (left) and valley (right) for different values of reference wind speed U_{10} and reference rainfall intensity R.

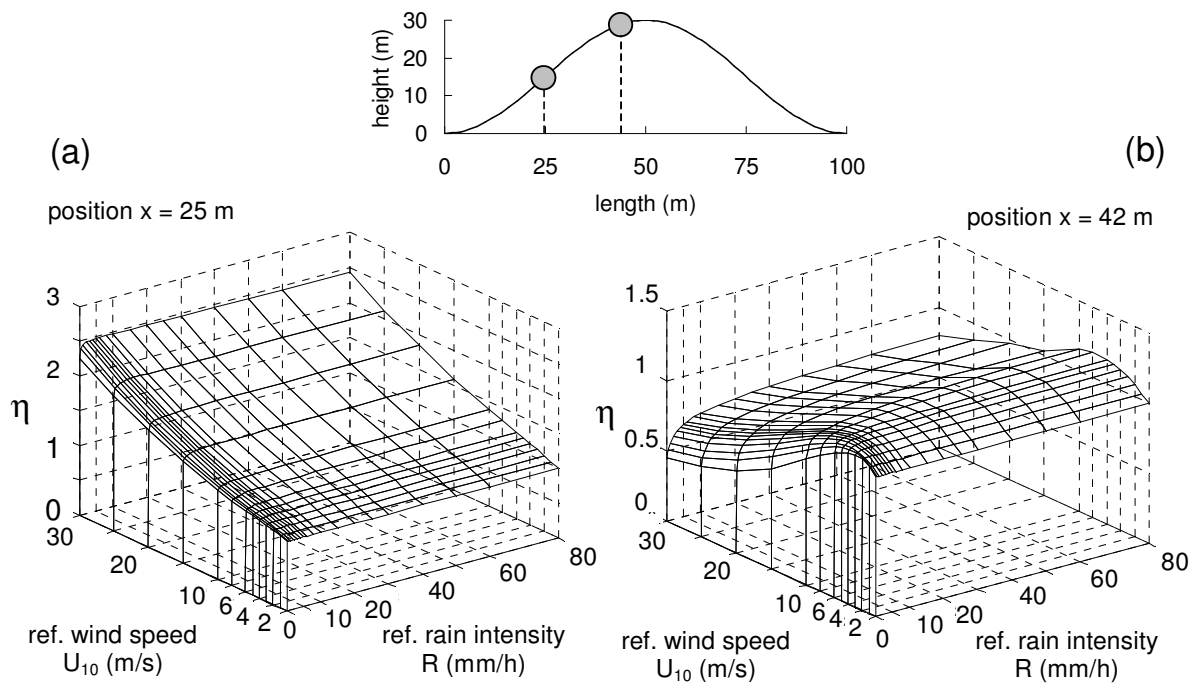

Fig. 14. Catch ratio charts giving η as a function of reference wind speed U_{10} and reference rainfall intensity R for (a) position x = 25 m and (b) position x = 42 m on the hill surface.

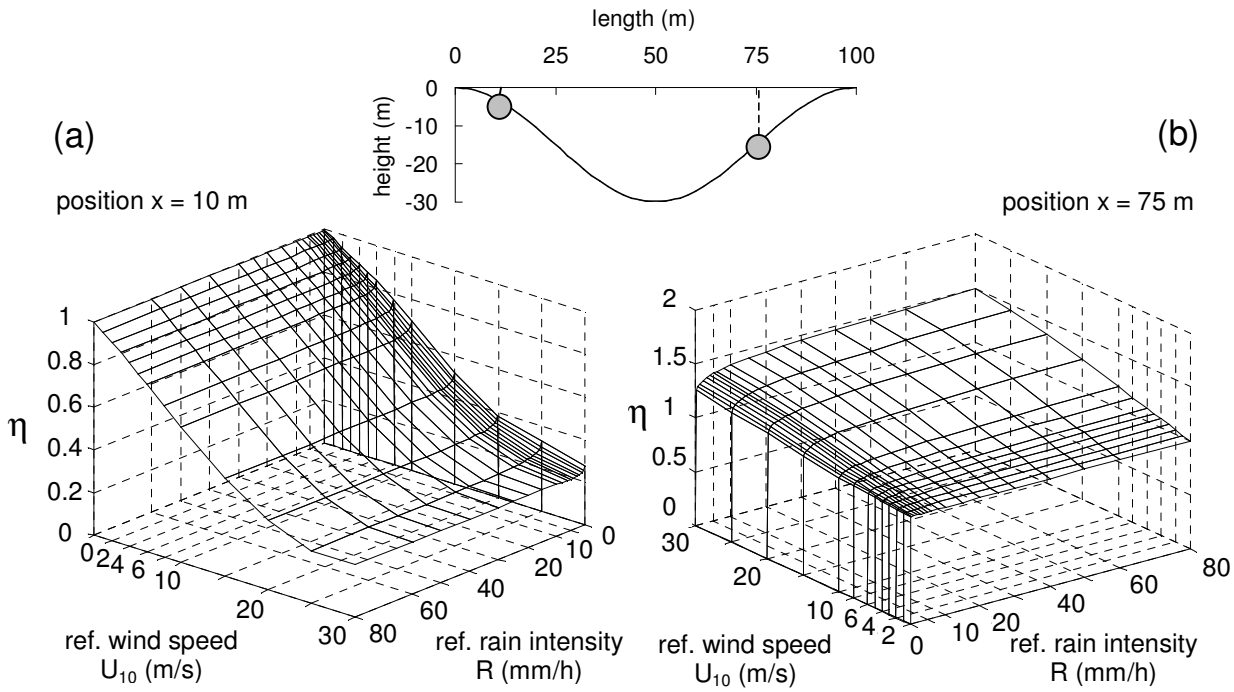

Fig. 15. Catch ratio charts giving η as a function of reference wind speed U_{10} and reference rainfall intensity R for (a) position x = 10 m and (b) position x = 75 m on the valley surface.

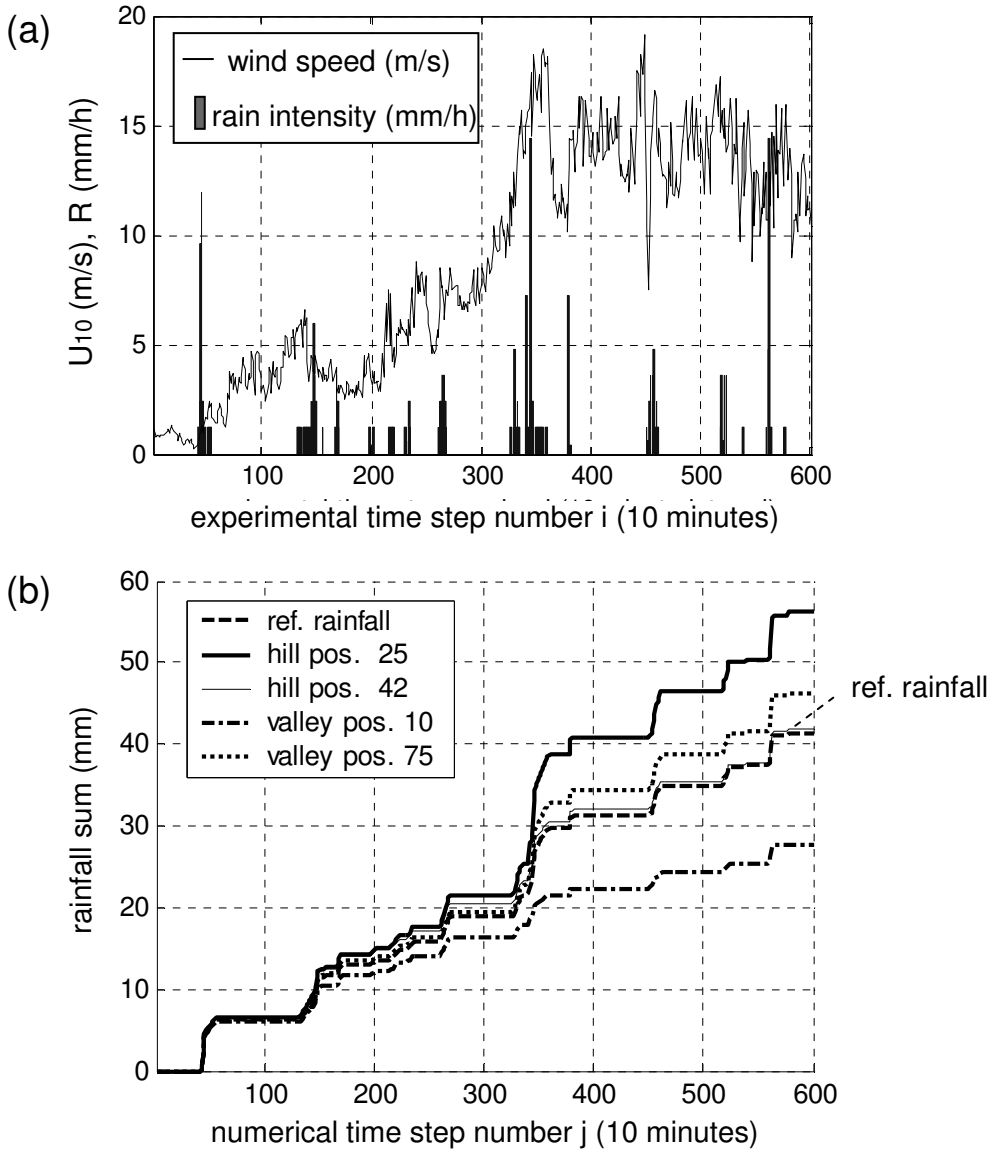

Fig. 16. (a) Meteorological data record for an example rain event. Data values of reference wind speed U_i and reference rainfall intensity R_i are given for each experimental time step i (= 10 minutes) in the 4-day rain event. Total reference rainfall sum S = 41 mm. (b) Temporal distribution of the reference meteorological rainfall sum and the hydrological rainfall sums during the rain event. The hydrological rainfall sums impacting at positions x = 25 m and x = 42 m on the hill surface and at positions x = 10 m and x = 75 m on the valley surface are displayed. The positions are indicated in Fig. 14 and 15.

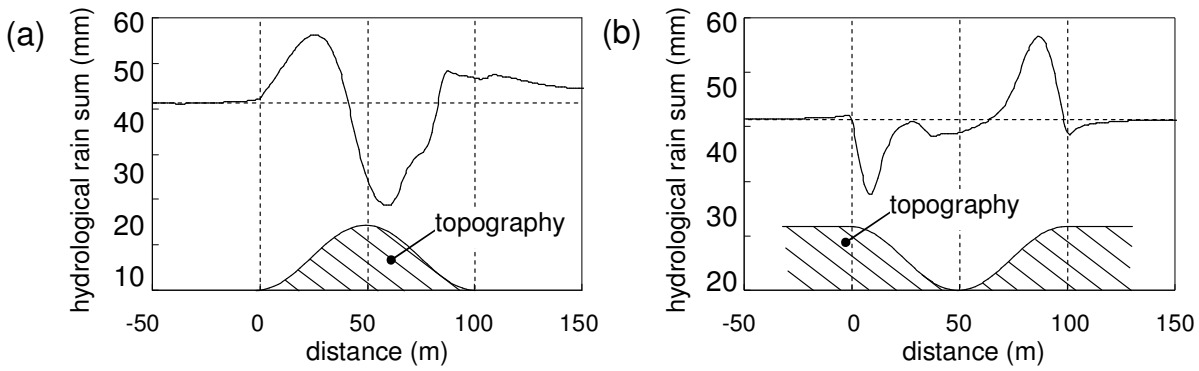

Fig. 17. Spatial distribution of the hydrological rainfall sum at the end of the rain event given in Fig. 16a. The topography is indicated in the bottom of the figure (hatched). The reference meteorological rainfall sum is 41 mm and is indicated by the dashed horizontal line.